Geophysical Research Letters

RESEARCH LETTER
10.1029/2019GL083687

The Impact of Wind Gusts on the Ocean Thermal Skin Layer

Christopher J. Zappa[1], **Nathan J. M. Laxague**[1], **Sophia E. Brumer**[2], and **Steven P. Anderson**[3]

[1]Lamont-Doherty Earth Observatory, Columbia University, Palisades, NY, USA, [2]Laboratoire d'Océanographie Physique et Spatiale, UMR 6523 IFREMER-CNRS-IRD-UBO, Plouzané, France, [3]Areté Associates, Arlington, VA, USA

Key Points:
- Wind gusts produce transient ocean skin layer thermal fronts that propagate near the observed wind speed
- Wind gust fronts disrupt the ocean thermal skin layer due to microbreaking and increase emissivity due to capillary-gravity wave growth
- Following wind gust front passage, capillary-gravity wave relaxation reduced surface emissivity faster than the cool skin was restored

Supporting Information:
- Supporting Information S1

Correspondence to:
C. J. Zappa,
zappa@ldeo.columbia.edu

Citation:
Zappa, C. J., Laxague, N. J. M., Brumer, S. E., & Anderson, S. P. (2019). The impact of wind gusts on the ocean thermal skin layer. *Geophysical Research Letters*, *46,* 11,301–11,309. https://doi.org/10.1029/2019GL083687

Received 11 MAY 2019
Accepted 22 AUG 2019
Accepted article online 27 AUG 2019
Published online 28 OCT 2019

Abstract The thermodynamic and emissive properties of the ocean thermal skin layer are crucial contributors to air-sea heat flux. In order to properly observe ocean surface temperature without disturbing any delicate fluid mechanical processes, thermal infrared imaging is often used. However, wind impacting the ocean surface complicates the extraction of meaningful information from thermal imagery; this is especially true for transient forcing phenomena such as wind gusts. Here, we describe wind gust-water surface interaction through its impact on skin layer thermal and emissive properties. Two key physical processes are identified: (1) the growth of centimeter-scale wind waves, which increases interfacial emissivity, and (2) microscale wave breaking and shear, which mix the cool skin layer with warmer millimeter-depth water and increase the skin temperature. As more observations are made of air-sea interaction under transient forcing, the full consideration of these processes becomes increasingly important.

Plain Language Summary When a wind gust impacts an air-water interface, two separate processes work to increase the temperature sensed by an infrared camera. The shortwave-roughened surface becomes more emissive, and the skin layer (upper tens to hundreds of micrometers) becomes warmer as it is mixed by microscale wave breaking. The present paper identifies the effects of both processes in a field observational data set. This work is important to the quantification of air-sea heat flux from thermal infrared measurements.

1. Introduction

The ocean thermal boundary, or skin, layer (Ewing & McAlister, 1960; Saunders, 1967; Woodcock, 1941; Woodcock & Stommel, 1947) is critical to the transfer of heat between the ocean and the atmosphere. The temperature difference across the skin layer, ΔT_{skin}, is dependent on the net heat flux and the thickness of the aqueous thermal boundary layer, which is related to the wind stress (Saunders, 1967). The quantity ΔT_{skin} is defined as the skin sea surface temperature (SST) minus the subskin SST (Jessup et al., 2009). The skin SST (T_{skin}) is the radiometric temperature measured across a very small depth of approximately 20 μm. The subskin SST (or $T_{subskin}$) represents the temperature at the base of the thermal skin layer (~1,000 μm; Donlon et al., 2014; Donlon et al., 2007). Typically, the ocean has a cool skin layer, with the skin temperature being lower than that of the water immediately below (Katsaros, 1980).

Measurements of the thermal properties of the ocean skin layer are typically made with instruments sensitive to infrared (IR) electromagnetic radiation. As such, the emissivity ε of the ocean surface is critical to the estimate of skin temperature (Donlon et al., 2014). Canonical values for ocean emissivity are determined from the Fresnel complex index of refraction (Downing & Williams, 1975; Friedman, 1969). Additionally, the emissivity of the ocean surface depends on electromagnetic wavelength and incidence angle according to the Fresnel equations, temperature/salinity (Newman et al., 2005), and ocean surface capillary-gravity waves (Henderson et al., 2003; Masuda et al., 1988).

Near-surface ocean turbulence manifests itself as disruptions of the cool skin layer, bringing warmer subskin water to the surface. This idea has been utilized to remotely quantify wave breaking dynamics of whitecapping (Jessup et al., 1997) and to detect and quantify microbreaking, the breaking of small-scale waves which does not entrain air (Jessup et al., 1997). Furthermore, it has been used to quantify the influence of microbreakers on air-sea gas transfer (Zappa et al., 2001; Zappa et al., 2004). The cool skin layer has been shown to

recover from disruptions as a function of the net heat flux and strength of the turbulent disruption relative to the background turbulence (Zappa et al., 1998). Simpson and Paulson (1980) observed the ocean surface skin layer to thin on the upwind face of dominant gravity waves and suggested this to be due to enhanced wind stress. Furthermore, they observed similar thinning immediately downwind of the crests of steep short gravity waves and suggested this to be due to surface instability. Jessup and Hesany (1996) proposed that small-scale wave breaking due to longwave/shortwave interaction may dominate the modulation of ocean skin temperature by swell waves. Disturbances of the cool skin layer caused by small-scale Langmuir turbulence have been shown to increase the heat transfer across the air-sea interface (Veron & Melville, 2001). Despite these ubiquitous disturbances, the presence of an average ΔT_{skin} has been observed to persist at wind speeds of up to 20 m/s (Donlon et al., 1999).

Even without turbulent disruptions of the cool skin layer, electromagnetic modulation of the surface emissivity will cause changes in the observed brightness temperature. The surface emissivity is insensitive to changes in incidence angle, θ_i, for $\theta_i < 40°$, although it becomes increasingly sensitive for greater values of θ_i (Downing & Williams, 1975). For low incidence angle viewing, the average radiance is found to be independent of ocean surface roughness. For high incidence angle viewing, the sensed radiance will increase with roughness, even if the skin temperature remains the same (Saunders, 1968). The emissivity of fresh water and seawater has been modeled for varying sea surface roughness as a function of the incidence angle and the surface wind speed in the infrared window regions, 3.5–4.1 and 8–13 μm. The effect of surface wind was found to greatly affect emissivity for incidence angles >70° (Henderson et al., 2003; Masuda et al., 1988; Wu & Smith, 1997). This behavior in emissivity was observed in field measurements determined over the 8- to 12-μm window at incidence angles of 40° and 55° at wind speeds up to 13 m/s (Hanafin & Minnett, 2005).

Here, we examine the transient wind forcing on the water surface and the response of the thermal skin layer. While the measurements herein were performed in an estuarine system, we expect the relevant dynamics to be general and most applicable in the ocean environment. Additionally, we do not focus on the larger-scale atmospheric dynamics that generate wind gusts such as deep convection, downdrafts, and flow convergence in the atmospheric boundary layer. Figure 1 schematically shows the processes relevant to thermal imaging at the air-sea interface prior to and following a wind gust. A net outward heat flux sets up an ocean skin layer where the skin temperature (at 10 μm) is colder than the subskin water immediately below (at 1 mm). Following the wind gust, the surface roughens, which leads to an increased brightness temperature from both an increase in emissivity and direct disruption of the cool skin layer due to shear and microscale wave breaking that mixes warmer water up to the surface. Our results show that the observed response of the thermal skin layer is both thermodynamic/hydrodynamic and electromagnetic in nature. In the work that follows, we present results for both the physical processes important to thermal imaging of wind-roughened ocean surfaces and the general propagation of wind gust fronts in the wind direction.

2. Materials and Methods

2.1. Study Area

Field observations were made on the Hudson River on the nights of 18 and 19 November 2010 during ebb tides. One set of imaging measurements was made from the State Line Lookout in the Palisades Interstate Park, NJ, approximately 32 km north of Manhattan. Another set of imaging measurements were made from aboard a barge that was moored in the river within the cliff-based imager field of view (FOV) during acquisition. The region of interest for this study lies outside of the tidal channel, in a region of relative bathymetric uniformity where the water depth varied between 3.8 and 5.2 m during the survey period.

2.2. Data and Instrumentation

The State Line Lookout camera system consisted of a 1,024 by 1,024 pixel midwave IR (MWIR) camera (FLIR System SC8000; 3–5 μm). The MWIR camera was fitted with a 50-mm lens providing a 20.6° horizontal by 20.6° vertical FOV. MWIR imagery was collected at 16 Hz and provides better than 25-mK temperature resolution.

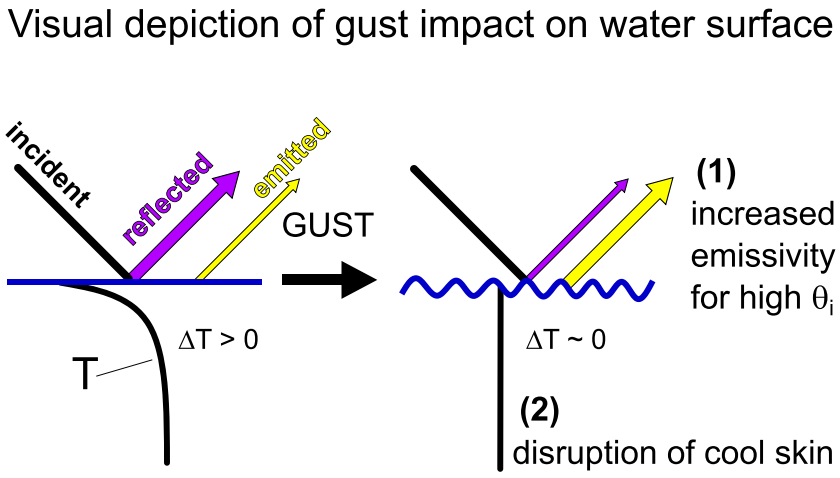

Figure 1. Two key physical processes at play as a gust impacts the water surface: (1) roughening of air-water interface due to incipient growth of short-scale waves, increasing emissivity of the surface. (2) Fluid mechanical disruption of cool skin layer due to shear processes and microscale wave breaking, increasing skin temperature.

The cameras were mounted on a heavy bench and anchored after initial alignment. The camera location was surveyed with GPS to an accuracy of 10 cm. (40.98829°N, 73.90612°W at 131.87-m WGS-84). The camera was pointed at 23.2 clockwise from due north. In the FOV of the cameras is an instrumented piling containing an array of sensors located at 40.98958°N, 73.90204 W. At an elevation of approximately 155 m above the water surface with a mean incidence angle, θ_i, of 65° (54.7–75.3°), the nominal MWIR ground sample distance was 13 cm by 31 cm with an image swath on the river surface of 133 m by 372 m, while the ground sample distance of the visible camera is 9 cm by 22 cm with an image swath on the water of 412 m by 1,314 m. A constant camera roll (tilt) offset was determined from fiducial markers in the FOV.

At the start of each half hour collection, hot and cold calibration plates were placed in front of the MWIR camera sequentially. These data were used for nonuniformity corrections and also removed banding in the images. The lens distortion was measured in an optics laboratory prior to deployment, and corrections were applied in postprocessing. The images were then mapped to the water surface with bilinear interpolation using the time-varying elevation of the water surface provided by a U.S. Geological Survey gauge located at Hastings-On-Hudson. The mapping resolution was 0.2 m. Finally, 16-Hz mapped images were downaveraged to 4 Hz.

Concurrent with the cliff-based MWIR image acquisitions, a series of 10-min longwave IR (LWIR) videos were taken of the river surface from the R/V Marguerite Miller that was moored near the piling with various instruments mounted for atmospheric and subsurface measurements (Brumer et al., 2016). The LWIR data were collected every 30 min between 0100 and 0600 UTC on 18 November and 0400–1000 UTC on 19 November for a total of 23 runs. The CEDIP model Jade III longwave (8.0–9.3 μm) camera was mounted ~5.5 m above the water level with an incidence angle of approximately 25°. This setup permitted the LWIR camera to always view upstream of the barge into the tidal current. An Xsens Inertial Measurement Unit was mounted next to the camera to measure the pitch and roll of the barge motion at a frequency of 10 Hz, allowing for projection correction. The FOV of the camera was 21.7° × 16.4°, giving an image area of 4.6 m^2 with an average pixel size of 0.6 cm^2. The CEDIP Jade III was sampled at 60 Hz and provides better than 15-mK temperature resolution with 320 × 240 pixels.

Atmospheric boundary layer processes were sampled using a Campbell air-sea flux package set atop a piling in the middle of the river at a height of 7.5 m from the riverbed. Relevant to this study, the wind velocity was measured at 2.3–3.7 m above the mean water level. The sky brightness temperature was measured with a Heitronics model KT-15 (8–14 μm) radiometer from both the barge and the cliff at the corresponding zenith angles. Broadband longwave downwelling (sky) radiation was measured at the piling using a Kipp and Zonen model CGR4 (4–40 μm) pyrgeometer. The ship remained within 130 m of the piling during data collection.

2.3. Radiometric Calculations

We compute spectral radiance of an object for wavelength λ at temperature T using Planck's law, $B(\lambda,T)$. By integrating spectral radiance between high and low wavelength limits (determined by instrument spectral response), we obtain the radiance in Watts·steradian^{-1}·meter^{-2}

$$L(T) = \int_{\lambda_{\text{low}}}^{\lambda_{\text{high}}} B(\lambda, T)\, \mathrm{d}\lambda \tag{1}$$

The radiance sensed by one of the infrared cameras in our setup is dependent upon the water-leaving radiance, the sky-leaving radiance, and the surface emissivity

$$L_{\text{water,platform}} = \epsilon_{\text{platform}} L_{\text{water,skin}} + \left(1-\epsilon_{\text{platform}}\right) L_{\text{sky,platform}} \tag{2}$$

where the subscript "platform" refers to either barge or cliff. Using Planck's law, we compute $L_{\text{water,barge}}$ and $L_{\text{sky,barge}}$ given the observed surface and sky brightness temperatures, respectively. $L_{\text{sky,platform}}$ increases with increasing zenith angle because the sensor measures more of the warm atmospheric surface layer along the path. Additionally, clouds (which are strong absorbers) will also increase $L_{\text{sky,platform}}$ because they exist in the lower troposphere and are therefore warmer than an open patch of sky that extends into the stratosphere. Independent of changes to emissivity, these effects will both increase the observed radiance from the water surface.

3. Results

We present a case study to demonstrate the impact of transient wind forcing on the air-water interface and the response of the thermal skin layer. Figure 2 shows MWIR imagery from the cliff and LWIR imagery barge-based systems during the passage of a single thermal front (see supporting information Movie S1; note the observed bursts passing through the imagery that propagate for O(10 s) duration or more). The cliff-based images have incidence angles ranging from 54.7° to 75.3°, and the barge images have incidence angles ranging from 17° to 33°. The cliff-based MWIR images show surface gravity waves roughly 3 m in wavelength propagating from the upper left corner toward the bottom right. The waves are more prominent at the top of the imagery where the reflectivity is greater. Note the warm wakes generated by the meteorological piling; these denote that a cool skin layer exists and indicate the direction of the surface current. Also, note the warm reflection of the piling in the MWIR cliff-based imagery. The red trace in the cliff-based imagery, determined by edge detection (described in the supporting information) and confirmed by manual inspection, highlights a thermal front at the water surface propagating across the imaged region.

The higher resolution barge-based LWIR images show classic fine-scale turbulent eddies impacting the skin layer and ordered scalloped disruptions as the thermal front propagates over the barge (see supporting information Movie S1). The middle panel in Figure 2 shows a time series of the average water surface brightness temperature computed over the whole barge image FOV and for the colocated barge region in the cliff-based imagery. Before the thermal front passes the barge, the mean brightness temperature sensed by the barge-based camera was roughly 0.8 °C warmer than it was for the cliff-based camera. This mean difference is attributed to the difference in emissivity of the water surface between the two camera systems. For the barge LWIR camera with a spectral response between 8 μm $< \lambda <$ 9.3 μm at $\theta_i = 25°$, $\varepsilon_{\text{barge}} = 0.985$; for the cliff MWIR camera with a spectral response between 3 μm $< \lambda <$ 5 μm at $\theta_i = 67°$, $\varepsilon_{\text{cliff}} = 0.876$ (Downing & Williams, 1975). As the thermal front passes through the imaged patch on the water surface, both the cliff- and barge-based cameras show a slight dip in brightness temperature. Immediately afterward, a sharp increase in brightness temperature is observed in both camera systems. Following the passage of the thermal front, this increase persists in the barge-based time series but decreases with time in the cliff-based time series.

The physical property sensed by both of the IR cameras is the water skin temperature. The LWIR barge incident angle is small so the emissivity is not very sensitive to roughness, but the MWIR cliff incident angle is larger and thus more sensitive to roughness. This incident angle disparity enables a derivation of time-varying emissivity for the MWIR cliff images. The skin temperature at the barge is determined

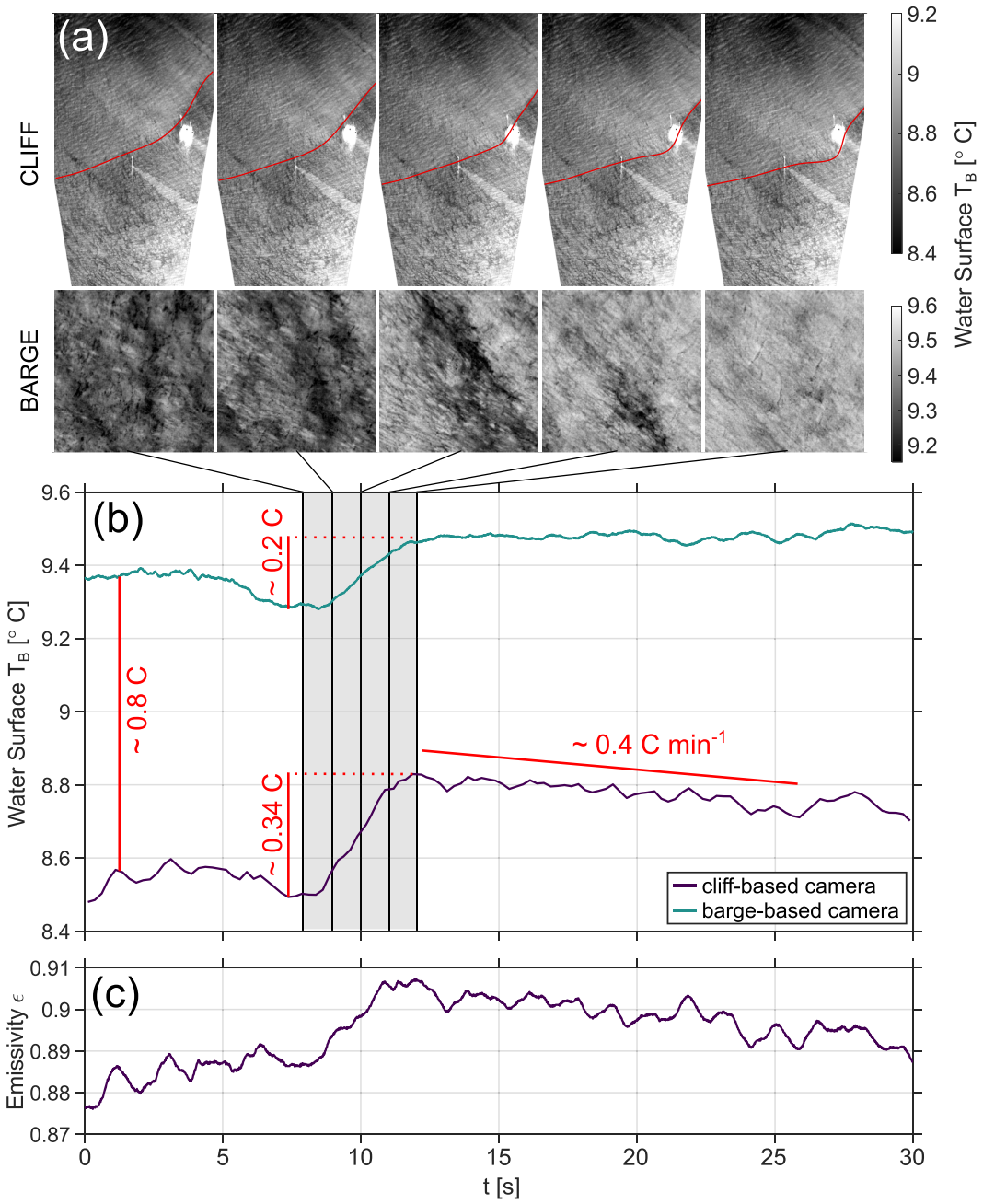

Figure 2. Example of thermal front propagation as viewed by cliff-based and barge-based IR cameras. (a) Time series of thermal imagery. Color bars indicate brightness temperature in degrees Celsius. The red trace highlights the thermal front at the water surface propagating across the imaged region. (b) Time series of mean surface brightness temperature around time at which thermal front propagates by barge. (c) Time series of cliff-based camera emissivity computed from the two infrared cameras and the skyward-looking radiometers.

using equation (2) given the observed barge brightness temperature, observed sky temperature at the corresponding zenith angle, and a constant emissivity, $\varepsilon_{barge} = 0.985$ (which does not change for $\theta_i < 40°$; Downing & Williams, 1975). The temporal changes in MWIR emissivity for the cliff-based sensor may then be derived using (2) given the skin temperature measured at the barge, the observed cliff-based brightness temperature, and the sky temperature at the corresponding cliff zenith angle. The bottom of Figure 2 shows the temporal variability in the derived MWIR emissivity. The derived MWIR emissivity shows an increase which is coincident with the initial increase in brightness temperatures seen in both cameras.

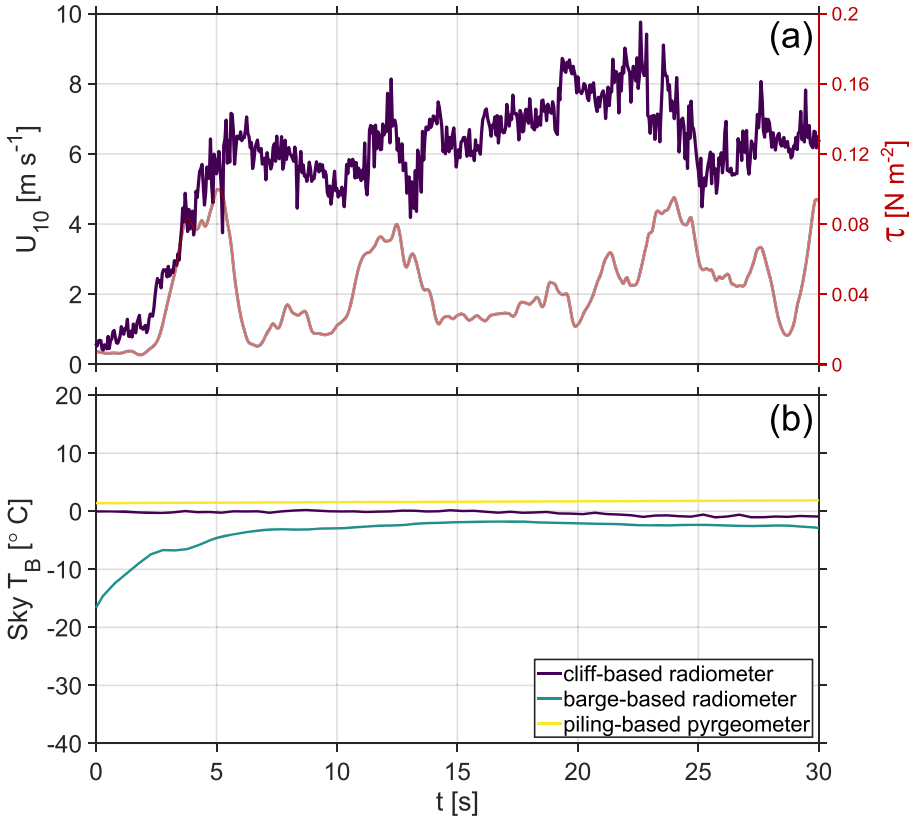

Figure 3. Time series of (a) 10-m wind speed as determined from piling-mounted sonic anemometer (black) and wind stress computed from wavelet coscalograms (Laxague et al., 2018), subjected to a 1-s moving median filter. (b) Sky temperature as determined from upward-looking KT-15 radiometers mounted on the cliff (violet) and barge (teal) as well as the pyrgeometer (yellow) mounted at the meteorological piling.

At the time that the thermal front passed the barge, the meteorological station on the piling recorded a dramatic increase in wind speed, that is, a wind gust (Figure 3a). Using the peak wavelet amplitude technique (Laxague et al., 2018), the wind stress time series was estimated from the along-stream and vertical wavelet coscalograms. Data from the cliff-based and barge skyward-looking infrared radiometers as well as the piling-based pyrgeometer show that the sky temperature did not vary much during the time of interest (Figure 3b). Based on the sky brightness temperature of approximately −3 to 1.5 °C, the sensors were likely sampling the relatively warm lower atmosphere for an overcast sky.

We analyzed 20 gusty wind forcing periods with similar thermal front propagation behavior shown in this case study. For each case, the thermal front propagation speed was determined (see supporting information) and compared with the median wind speed over that time period. This information is shown in Figure 4: in (a) as two distributions computed over a representative wind gust front passage and in (b) as a comparison of median thermal front propagation speed and wind speed for all wind gust front passages. There is good agreement between these two speeds computed from both sources ($R^2 = 0.68$), with the speeds of the thermal front propagation slightly less than those of the wind for greater values of wind speed (line of best fit sloped 0.77).

4. Discussion

The temporal developments shown in Figures 2 and 3 indicate the passage of a water surface thermal front which coincided with a rapid increase in wind speed. The wind stress time series (Figure 3a) shows that this increase in wind speed dramatically increased the wind stress for approximately 5 s. The slightly reduced brightness temperature which precedes the thermal front shown in Figure 2b is owed to the immediate increase in latent and sensible heat flux which results from the initial wind gust prior to any disruption of

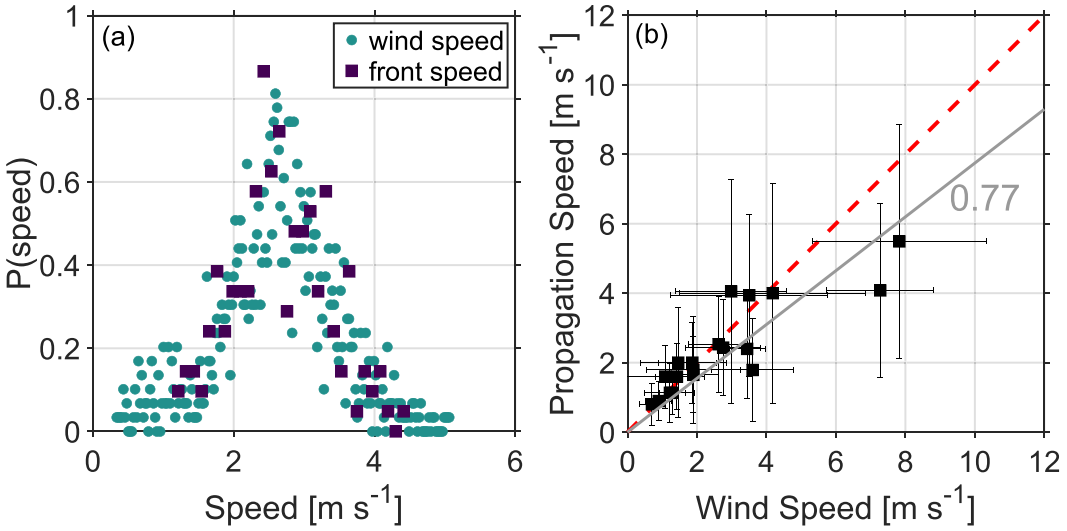

Figure 4. (a) Probability density functions of thermal front propagation speed and wind speed for a representative wind gust front event. (b) Comparison of median wind speed and median thermal front propagation speed for all cases, where bars indicate one standard deviation. Coefficient of determination $R^2 = 0.68$ for 1:1 comparison and $R^2 = 0.79$ for line of best fit, sloped at 0.77.

the cool skin layer (Veron & Melville, 2001). The impulsive wind stress grows and steepens short capillary-gravity waves that roughen the surface and lead to the disruption of the thermal boundary by shear processes and microbreaking. This physical disruption affected the brightness temperature of both the barge- and cliff-based imagery (see supporting information Movie S1). Notice the elongated thermal features which are oriented along the wind gust propagation direction in the barge-based imagery. These are consistent with what one would expect after the scalloped mixed regions resulting from microscale breaking are stretched in the wind direction (Jessup, Zappa, & Yeh, 1997; Zappa et al., 2004). In addition, the roughened surface resulted in an increased emissivity at the high incidence angles for the cliff imagery; this emissivity effect was not substantial at low incidence angle for the barge imagery (Masuda et al., 1988). Therefore, the increase in brightness temperature in the barge imagery of 0.2 °C is due to disruption of the skin layer alone (and would equate to ΔT_{skin} assuming the disruption is complete), while the cliff-based imagery increase of 0.34 °C is due to both disruption and electromagnetic effects (i.e., increased emissivity due to increased surface roughness). Indeed, closer inspection of the meteorological piling's wake shows that the disruption induces a 0.2 °C temperature difference (see Figure S1) that corresponds to ΔT_{skin}. The increase in surface brightness temperature in the cliff-based imagery due to increased emissivity is 0.14 °C, corresponding to a derived emissivity change of 0.02 using (2) as observed in Figure 2 bottom. This emissivity change due to wind forcing is higher than predicted by Masuda et al. (1988), who modeled a negligible wind-induced change to emissivity at $\theta_i = 67°$. However, our results are comparable with those of Henderson et al. (2003) who predicted an emissivity of 0.015 for our measurement conditions. A reasonable explanation for this finding is that the young, strongly forced waves at the wind gust front are steeper on their downwind face (i.e., more skewed) than they would be for fully developed seas in equilibrium with the wind. The cliff-based camera looking into the wind direction therefore sees the strongly sloped downwind faces of the shortwaves, increasing the emissivity.

The increase in brightness temperature due to a wind gust front has been shown to be the result of the skin layer disruption by microbreaking and shear in the LWIR regime at low to moderate incidence angles and of the combined effects of skin layer disruption and increased emissivity with surface roughness at high incidence angle in the MWIR regime. The intensity of the wind gust front may impact the strength of the disturbing physical processes (i.e., microbreaking and shear) and therefore the strength and duration of skin layer disruptions (Jessup et al., 2009; Zappa et al., 1998). The intensity of the wind gust front will also impact the spatial extent of microbreaking and therefore the coverage of skin layer disruptions (Zappa et al., 2001; Zappa et al., 2004). Furthermore, the electromagnetic (EM) effect may be linked to the level of wind forcing in terms of the impact of wave growth on surface roughness and enhanced emissivity.

After the wind gust front had passed the area of interest, the brightness temperature in the cliff-based imagery decreased at a rate of 0.4 °C/min over ~20 s. However, the barge surface brightness temperature remained roughly constant due to a persistent mixing of the cool skin layer. This difference in behavior can be explained by a relaxation of short-scale waves that results in a reduction in emissivity as suggested by Masuda et al. (1988). This is supported by shortwave relaxation timescales of 0.1 to 10 s that are consistent with the literature (Caponi et al., 1988). Note that this rate of decrease in temperature will also depend on the strength of the original surface disturbance (Jessup et al., 2009; Zappa et al., 1998). Additionally, the downwelling irradiance did not vary during the observation period and the conditions were overcast as indicated in Figure S2. Indeed, Figure S3 shows that the observed changes in sky temperature—given either specular reflection or diffuse scattering (e.g., Niclòs et al., 2007)—are not responsible for the decrease in surface brightness temperature. This description of the event fits with theory and past observations of how waves impact surface emissivity and disrupt the cool skin layer and effectively explains the disparate cliff-based and barge-based views of the phenomenon.

As the two camera systems have different spectral sensitivities, they represent the photons emitted from slightly different layers of the water skin layer. Specifically, the *e*-folding depth in water for 3- to 5-μm wavelength EM radiation (the cliff-based camera) is 35.2 μm (Downing & Williams, 1975). For 8- to 9.3-μm wavelength EM radiation (the barge-based camera), it is 17.9 μm (Downing & Williams, 1975). This effect is likely of second-order importance: Even for a sharp aqueous skin layer vertical temperature gradient of order 1 °C/mm (Ewing & McAlister, 1960; Katsaros, 1980; Saunders, 1967; Woodcock & Stommel, 1947), the two camera systems would differ in their observation of skin temperature by order 0.01 °C. This is an order of magnitude smaller than the brightness temperature increase observed during the wind gust front passage.

The phenomena described here are general in nature and are expected to occur in the ocean environment. However, the presence of dissolved salts in the ocean is known to play a role in infrared remote sensing of skin temperature. Typical ocean skin layer vertical salinity gradients are on the order of 1 practical salinity unit (psu)/mm (Zhang & Zhang, 2012). In the event of a wind gust which disrupts the saline sublayer, we would expect a reduction in skin salinity of 0.05–0.15 psu. It has been shown that the change in LWIR emissivity from fresh water (0 psu) to ocean water (35 psu) is of order 0.001 (Friedman, 1969; Newman et al., 2005; Pinkley & Williams, 1976). The change in emissivity for ~0.1 psu should be negligible. Therefore, we expect the role of salinity in processes described here to be of minimal importance to infrared sensing when compared with the phenomena of wave growth and thermal disruption via breaking.

5. Conclusions

We have presented the observation of water surface thermal front passages from two different infrared imaging platforms. Measurement of the sky brightness temperature and a comparison of wind and thermal front propagation speeds allowed us to deduce that the imaged front was the result of wind forcing on the water surface. The observations represented here fit the description of the air-water interface when subjected to transient wind forcing. Two physical processes were identified in those observations: The roughening of the surface through wave growth increases emissivity at large incidence angles; microscale wave breaking and shear lead to the fluid mechanical disruption of the cool skin layer and mixing with warmer millimeter-depth water, presenting a thermal signature which is sensible at all incidence angles.

Understanding the thermodynamic processes at play in the aqueous thermal skin layer is essential to the proper description of air-sea heat flux. As technological development enables the widespread usage of thermal infrared imaging in this field, it is important to take into account the different physical processes which ultimately impact the observations. The present work was designed to serve in partial fulfillment of that purpose and is intended to support future studies of the role of wind gusts in air-sea interaction.

Acknowledgments
The authors first acknowledge John Dugan posing the question of the phenomenology causing the gust signatures in the infrared imagery. The authors thank Cindy Piotrowski, Seth Zuckerman, Kenneth Vierra, Mike Marnon, Kyle Bisson, and Zandy Williams from Areté Associates and Scott Brown and Deborah LeBel of Lamont-Doherty Earth Observatory for their assistance and support during the field work in Hudson River and with data preparation. The authors thank Miller's Launch for providing the crew boat Marguerite Miller and for their assistance onboard and the Palisades Interstate Park Commission for providing access to State Line Lookout. The authors gratefully acknowledge support from the Office of Naval Research Awards N00014-11-1-0922 and N00014-15-1-2153 for the Lamont-Doherty Earth Observatory and N00014-13-C-0387 for Areté Associates. S. E. B. is supported by a postdoctoral grant of the Centre National d'Études Spatiales (CNES). Data used in the analysis described here have been made available through the Columbia Academic Commons (http://doi.org/10.7916/d8-zqp3-fn39). This is Lamont-Doherty Earth Observatory contribution 8350.

References

Brumer, S. E., Zappa, C. J., Anderson, S. P., & Dugan, J. P. (2016). Riverine skin temperature response to subsurface processes in low wind speeds. *Journal of Geophysical Research: Oceans*, *121*, 1721–1735. https://doi.org/10.1002/2015JC010746

Caponi, E. A., Crawford, D. R., Yuen, H. C., & Saffman, P. G. (1988). Modulation of radar backscatter from the ocean by a variable surface current. *Journal of Geophysical Research*, *93*(C10), 249–263.

Donlon, C., Robinson, I., Casey, K. S., Vazquez-Cuervo, J., Armstrong, E., Arino, O., et al. (2007). The global ocean data assimilation experiment high-resolution sea surface temperature pilot project. *Bulletin of the American Meteorological Society*, *88*(8), 1197–1214. https://doi.org/10.1175/BAMS-88-8-1197

Donlon, C. J., Minnett, P. J., Jessup, A. T., Barton, I., Emery, W., Hook, S., et al. (2014). Ship-borne thermal infrared radiometer systems. *Experimental Methods in the Physical Sciences: Optical Radiometry for Ocean Climate Measurements*, *47*(1), 305–404. https://doi.org/10.1016/B978-0-12-417011-7.00011-8

Donlon, C. J., Nightingale, T. J., Sheasby, T., Robinson, I. S., & Emery, W. J. (1999). Implications of the oceanic thermal skin temperature deviation at high wind speed. *Geophysical Research Letters*, *26*(16), 2505–2508. https://doi.org/10.1029/1999GL900547

Downing, H. D., & Williams, D. (1975). Optical constants of water in the infrared. *Journal of Geophysical Research*, *80*(12), 1656–1661. https://doi.org/10.1029/JC080i012p01656

Ewing, G., & McAlister, E. D. (1960). On the thermal boundary layer of the ocean. *Science*, *131*(3410), 1374–1376. https://doi.org/10.1126/science.131.3410.1374

Friedman, D. (1969). Infrared characteristics of ocean water (1.5-15μ). *Applied Optics*, *8*(10), 2073–2078. https://doi.org/10.1364/AO.8.002073

Hanafin, J. A., & Minnett, P. J. (2005). Measurements of the infrared emissivity of a wind-roughened sea surface. *Applied Optics*, *44*(3), 398–411. https://doi.org/10.1364/AO.44.000398

Henderson, B. G., Theiler, J., & Villeneuve, P. (2003). The polarized emissivity of a wind-roughened sea surface: A Monte Carlo model. *Remote Sensing of Environment*, *88*(4), 453–467. https://doi.org/10.1016/j.rse.2003.09.003

Jessup, A. T., Asher, W. E., Atmane, M., Phadnis, K., Zappa, C. J., & Loewen, M. R. (2009). Evidence for complete and partial surface renewal at an air-water interface. *Geophysical Research Letters*, *36*, L16601. https://doi.org/10.1029/2009GL038986

Jessup, A. T., & Hesany, V. (1996). Modulation of ocean skin temperature by swell waves. *Journal of Geophysical Research*, *101*(C3), 6501–6511. https://doi.org/10.1029/95JC03618

Jessup, A. T., Zappa, C. J., Loewen, M. R., & Hesany, V. (1997). Infrared remote sensing of breaking waves. *Nature*, *385*(6611), 52–55. https://doi.org/10.1038/385052a0

Jessup, A. T., Zappa, C. J., & Yeh, H. (1997). Defining and quantifying microscale wave breaking with infrared imagery. *Journal of Geophysical Research*, *102*(C10), 23,145–23,153. https://doi.org/10.1029/97JC01449

Katsaros, K. B. (1980). The aqueous thermal boundary layer. *Boundary-Layer Meteorology*, *18*(1), 107–127. https://doi.org/10.1007/BF00117914

Laxague, N. J. M., Haus, B. K., Ortiz-Suslow, D. G., & Graber, H. C. (2018). Quantifying highly variable air–sea momentum flux using wavelet analysis. *Journal of Atmospheric and Oceanic Technology*, *35*(9), 1849–1863. https://doi.org/10.1175/JTECH-D-18-0064.1

Masuda, K., Takashima, T., & Takayama, Y. (1988). Emissivity of pure and sea waters for the model sea surface in the infrared window regions. *Remote Sensing of Environment*, *24*(2), 313–329. https://doi.org/10.1016/0034-4257(88)90032-6

Newman, S. M., Smith, J. A., Glew, M. D., Rogers, S. M., & Taylor, J. P. (2005). Temperature and salinity dependence of sea surface emissivity in the thermal infrared. *Quarterly Journal of the Royal Meteorological Society*, *131*(610), 2539–2557. https://doi.org/10.1256/qj.04.150

Niclòs, R., Caselles, V., Valor, E., & Coll, C. (2007). Foam effect on the sea surface emissivity in the 8–14 μm region. *Journal of Geophysical Research*, *112*, C12020. https://doi.org/10.1029/2007JC004521

Pinkley, L. W., & Williams, D. (1976). Optical properties of sea water in the infrared*. *Journal of the Optical Society of America*, *66*(6), 554–558. https://doi.org/10.1364/JOSA.66.000554

Saunders, P. M. (1967). The temperature at the ocean-air interface. *Journal of the Atmospheric Sciences*, *24*(3), 269–273. https://doi.org/10.1175/1520-0469(1967)024<0269:TTATOA>2.0.CO;2

Saunders, P. M. (1968). Radiance of sea and sky in the infrared window 800-1200 cm (-1). *Journal of the Optical Society of America*, *58*(5), 645–652. https://doi.org/10.1364/JOSA.58.000645

Simpson, J. J., & Paulson, C. A. (1980). Small-scale sea surface temperature structure. *Journal of Physical Oceanography*, *10*(3), 399–410. https://doi.org/10.1175/1520-0485(1980)010<0399:SSSSTS>2.0.CO;2

Veron, F., & Melville, W. K. (2001). Experiments on the stability and transition of wind-driven water surfaces. *Journal of Fluid Mechanics*, *446*, 25–65.

Woodcock, A. H. (1941). Surface cooling and streaming in shallow fresh and salt waters. *Journal of Marine Research*, *4*(2), 153–161.

Woodcock, A. H., & Stommel, H. (1947). Temperatures observed near the surface of a fresh-water pond at night. *Journal of Meteorology*, *4*(3), 102–103. https://doi.org/10.1175/1520-0469(1947)004<0102:TONTSO>2.0.CO;2

Wu, X. Q., & Smith, W. L. (1997). Emissivity of rough sea surface for 8-13 μm: Modeling and verification. *Applied Optics*, *36*(12), 2609–2619. https://doi.org/10.1364/AO.36.002609

Zappa, C. J., Asher, W. E., & Jessup, A. T. (2001). Microscale wave breaking and air–water gas transfer. *Journal of Geophysical Research*, *106*(C5), 9385–9391. https://doi.org/10.1029/2000JC000262

Zappa, C. J., Asher, W. E., Jessup, A. T., Klinke, J., & Long, S. R. (2004). Microbreaking and the enhancement of air-water transfer velocity. *Journal of Geophysical Research*, *109*, C08S16. https://doi.org/10.1029/2003JC001897

Zappa, C. J., Jessup, A. T., & Yeh, H. H. (1998). Skin-layer recovery of free-surface wakes: Relationship to surface renewal and dependence on heat flux and background turbulence. *Journal of Geophysical Research*, *103*(C10), 21,711–21,722. https://doi.org/10.1029/98JC01942

Zhang, Y., & Zhang, X. (2012). Ocean haline skin layer and turbulent surface convections. *Journal of Geophysical Research*, *117*, C04017. https://doi.org/10.1029/2011JC007464